Plasmonics (2023) 18:769–779
https://doi.org/10.1007/s11468-023-01802-3

Numerical Analysis of Three-dimensional Nanodisk Array–based Surface Plasmon Resonance Biosensors for SARS-CoV-2 Detection

Yan Guo[1] · Xianglong Su[1] · Kaihua Wu[1] · Ken-Tye Yong[2]

Received: 10 January 2023 / Accepted: 7 February 2023 / Published online: 23 February 2023

Abstract
With continuous mutations of SARS-CoV-2 virus, new highly contagious and fast-spreading variants have emerged, including Delta and Omicron. The popular label-free immunosensor based on surface plasmon resonance (SPR) technique can be used for real-time monitoring of the ligand-analyte or antibody-antigen interactions occurring on the sensor surface. In this work, an SPR-based biosensor combined with a nanodisk array was presented to enhance the sensitivity toward virus detection. The nanodisk arrays were employed to enhance the adsorption of molecules for better detection by increasing the SPR field. Four optimal sensing configurations of silver or gold nanodisks on gold thin films with different aspect ratios were achieved through systematic optimization of all parameters to yield the best sensor performance. The resonance angle can be modulated simply by the aspect ratio of nanodisk array. The sensitivity of the optimized sensors has been improved, and the detection limit is smaller than that of bare gold-based sensor. The multi-jump resonance angle curves at tiny refractive index can clearly distinguish the difference of trace concentrations, which is very important for the accurate detection of trace substances.

Keywords Biosensor · Surface plasmon resonance · Nanodisk · Sensitivity · SARS-CoV-2 virus

Introduction

Coronaviruses (CoV) are a class of ribonucleic acid (RNA) viruses with similar structure envelopes [1]. The size of CoV varies from 60 to 140 nm in diameter with a single-stranded RNA nucleic acid genome [2]. Two widely recognized coronaviruses (severe acute respiratory syndrome (SARS) and Middle East respiratory syndrome (MERS)) are more virulent than known viruses specific to human coronaviruses, such as HKU1 [3]. These viruses have all caused severe respiratory infections around the world in the past two decades, with influenza-like symptoms but extremely deadly. Among these, SARS-CoV-2 is a new type of respiratory virus causing the severe acute respiratory syndrome, renamed as the novel coronavirus disease 2019 (COVID-19) by the World Health Organization since the end of 2019 [4, 5]. This virus led to the pandemic outbreak around the world owing to its rapid transmission between humans through direct and indirect contact, such as virions in airborne droplets causing severe symptoms like acute respiratory failure, severe pneumonia, pulmonary edema, and multiple organ failures, responsible for high mortality.

Since last year, cases of environmental transmission have been reported along with new types of mutations in the virus, such as Delta and Omicron, that led to the rapid increase in transmission rate [6]. Therefore, developing specific detection methods for real-time, rapid, accurate, and highly sensitive could prevent and control the transmission of SARS-CoV-2. Traditional methods for the diagnosis of respiratory viruses include direct isolation of the virus from cell culture, identification of the viral nucleic acid or antigen, and serological testing. But these detection technologies require high professionals and are time-consuming, not suitable for SARS-CoV-2 detection. Serological tests usually involve nucleic acid sequence amplification and long detection time. Alternatively, reverse transcription-polymerase chain reactions (RT-PCR) have become a common approach

✉ Yan Guo
guoyan@hdu.edu.cn

✉ Ken-Tye Yong
ken.yong@sydney.edu.au

[1] School of Automation, Hangzhou Dianzi University, Hangzhou 310018, China

[2] School of Biomedical Engineering, The University of Sydney, Sydney, Australia

for testing RNA viral cultures [7]. The detection procedure is simple consisting of extracting the viral nucleic acid from samples followed by transcription into complementary deoxyribonucleic acid (cDNA) and then amplification and analysis by fluorescence or luminescence techniques. As a result, the method has successfully been used for the diagnosis of a wide range of viruses, such as immunodeficiency virus (HIV) [8], hepatitis B and C viruses [9], and cytomegalovirus (CMV) [10]. These enveloped viruses are similar in structure with the surface containing envelope proteins, matrix proteins, and antigens, while the interior contains the genetic material [11]. But this kind of testing may lead to inaccurate outcomes since it amplifies non-specific sequences [12, 13].

Plasmonic detection based on surface plasmon resonance (SPR) may solve such shortcomings when applied to viral diagnostics. SPR technique can directly detect the intact form of insect pathogens through three biofunctional layers [14]. With the help of fusion proteins, the hepatitis B virus (HBV) can be detected by a gold-based SPR sensor chip [15], while the influenza A virus can also be detected by SPR generated by an ellipsometer [16]. Localized SPR biosensors can also detect avian influenza DNA hybridization [17]. With the development progress, the detection time is shortening. For example, the detection of immunoglobulin G (IgG) antibodies can be finished in three minutes [18]. Most importantly, SPR technology has already been used to detect MERS-CoV and SARS-CoV [19, 20], with SARS-CoV-2 showing about 79% and 50% identification of the sequences of SARS-CoV and MERS-CoV, respectively [21–23]. The main difference between these virions at the time of infection lies in the receptor. Similar to SARS-CoV, SARS-CoV-2 requires angiotension-converting enzyme 2 (ACE2) as a functional receptor to enter cells, while MERS-CoV needs dipeptidy1 peptidase 4 (DPP4). However, these viruses vary widely in terms of transmission speed and cure rates. For instance, MERS-CoV is not highly contagious but causes a very high mortality rate. The binding force of SARS-CoV-2 and ACE2 is 10–20 times that of the SARS virus [24], making SARS-CoV-2 the most contagious but with the lowest mortality rate. Therefore, the SPR method can be used to achieve rapid detection of SARS-CoV-2.

These above-mentioned viruses such as HIV and HBV share good similarities with SARS-CoV-2 particles in structure. Specifically, SARS-CoV-2 is an enveloped RNA virus containing four structural proteins in the envelope and a single-stranded RNA inside its structure as the genetic materials used as the most important biomarker for diagnosis of COVID-19 [25]. The four structural proteins are the spike surface glycoprotein (S), small envelope protein (E), matrix protein (M), and nucleocapsid protein (N), with S as the major antigen presented on SARS-CoV-2 surface critical for the virus to infect cells [15, 26]. However, SARS-CoV-2 structural and other accessory proteins, and even the whole virus SARS-CoV-2, could be used as antigens to monitor the coronavirus disease. Hence, SPR sensing structure can be employed to detect SARS-CoV-2 as reported by some studies. For example, graphene-coated platium-diselenide gold (Au) thin film was utilized to detect SARS-CoV-2 virus with different ligand-analyte achieving 183.3°/refractive index unit (RIU) [27]. Silicon and $BaTiO_3$ located on silver (Ag) film were employed to detect SARS-CoV-2 after growing a layer of thiol-tethered DNA to yield a sensitivity of 130°/RIU [28]. A layered structure based on two-dimensional (2D) material was employed to detect SARS-CoV-2 with a sensitivity of 194°/RIU [29]. Also, many studies employed local surface plasmon structures [30–32], and even exploit nanoparticle-enhanced SPR-sensing platforms to detect virus molecules contained in solution [33]. However, the preparation of such platforms is much more complex.

In the present work, a simple three-dimensional (3D) structure is constructed to improve the sensitivity and detection limit by changing the sensing interface. The structure and simulation techniques are described and the results are discussed.

Structure and Simulation Method

The conventional SPR-based biosensor scheme consists of a flat thin layer of plasmonic metal located on a prism with a large refractive index (RI), as well as an analyte solution for direct detection through contact with the other side of the plasmonic metal. To increase the contact area of the sensing interface and biomolecules, an array of nanodisks with regular distribution is directly laid on the top of the gold flat film. The diameter and height of the nanodisk are denoted by D and H, respectively. The separations between nanodisks in the X and Y directions are named by S_x and S_y, respectively. The work is started with square arrays ($S_x = S_y$) before studying the effect of aspect ratio. The employed light source originates from a He–Ne laser with a wavelength of 632.8 nm. The prism is based on BK7 with RI of 1.5151 at this wavelength. The nanodisk arrays with different parameters are located on the gold layer and are used to modify the topography of the chip surface. The configuration of the proposed sensing structure is shown in Fig. 1. The gold thin film with gold nanodisk arrays is functionalized with SARS-CoV-2 spike (S) protein antibody before adsorbing the SARS-CoV-2 virus in the serum/nasopharyngeal swab samples to act as the antigen contained in the analyte solution. The RI of the analyte solution is set to $1.3326 + dn$, where dn represents the RI change caused by the concentration of virus particles.

Many factors like the nanodisk material, size, and separations between them can influence the binding of the antigen

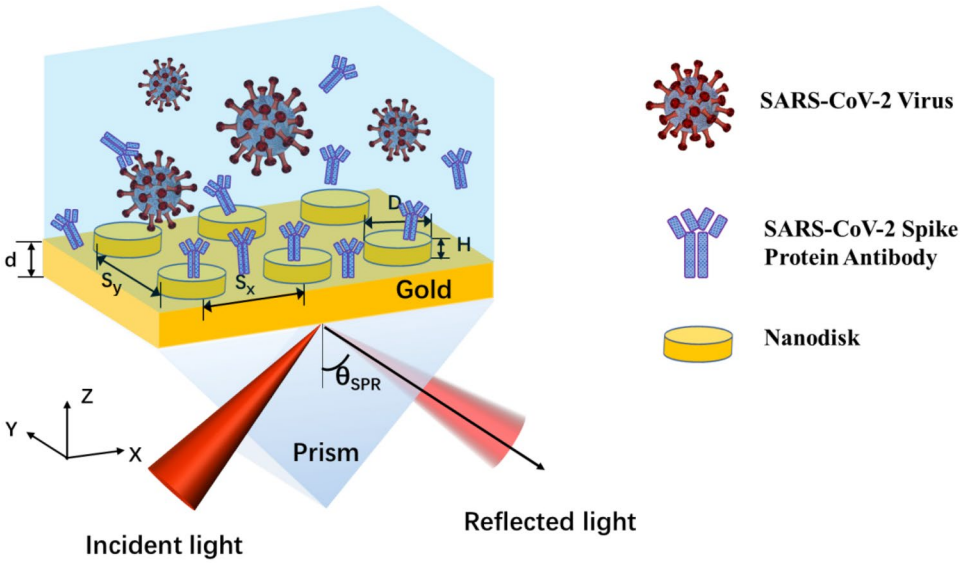

Fig. 1 The proposed SPR-based configuration to detect SARS-CoV-2 virus

and antibody, leading to different coupling electric fields and sensing performance. Hence, proper parameters would be essential to achieving maximum energy transfer from the incident light to the SPR for increasing the adsorption force to the target. For plasmonic metal, gold has often been used for ultra-thin structures due to its hard oxidation and corrosion. Silver may induce the most sensitive results but susceptible to oxidation. Since the conductivity of copper (Cu) is similar to that of silver, Cu can be used as a very good plasmonic metal but disadvantageous in terms of easy oxidation. Platinum (Pt) with good electrical conductivity and chemical stability at room temperature is used as an alternative to plasmonic metals. The RI data of these materials at the incident wavelength are given in Table 1. To achieve better sensing performance in 3D structures, the influence of the geometric parameters of the nanodisk array is investigated along with the effect of host materials.

In this work, the angle interrogation method is employed to find the best conditions for SPR biosensors. Several parameters can be utilized to evaluate the sensing performance. Among these, the incident angle θ is utilized as the input signal, which is changed as a function of the excited condition of SPR, and referred to SPR resonance angle when the corresponding reflectivity achieved a minimum value. The SPR field exponentially decays into the dielectric medium. Also, the distance at which the intensity reduced to 1/e corresponds to the skin depth of SPR, representing the influence scope of the SPR field. The detection accuracy of the sensing system is inversely proportional to the width of the resonance curve characterized by the full width at half maximum (FWHM) of the reflectivity curve. The sensitivity S is defined as the ratio of the differential SPR angle to the RI change of the sensing medium ($S = \Delta\theta / \Delta n$). The limit of detection (LOD) represents the minimum RI change caused by the lowest concentration of virus molecules triggering a significant response from the sensing system. For further commercialized sensing systems, the figure of merit (FoM) is utilized as the accuracy of concentration measurement of virus molecules, referred to the ratio of sensitivity to FWHM. Here, the FoM values of the optimized structures are compared to predict practicability.

Table 1 RI of the plasmonic metals at the wavelength of 632.8 nm

Materials	Refractive index (n)
Au	0.1377 + 3.6183i
Ag	0.056253 + 4.2760i
Cu	0.27 + 3.4081i
Pt	0.46695 + 6.1286i

Results and Discussion

COMSOL Multiphysics is used to build the model and simulate the reflection spectrum and electric field distribution. The combination of Au film and Au nanodisk (abbreviated as Au + Au) is first studied, with the parameter range of the nanodisk array limited within one incident wavelength. Using rough simulations, the height of nanodisk H is found very small. Otherwise, a waveguide mode is formed in the longitudinal direction of the nanodisks, suppressing the excitation of the surface mode in the lateral direction. The separation between nanodisks should also be large for better coupling the surface field (Supporting Information, Fig. S1a). The reflectivity curves of SPR for $H = 10$ nm and $D = 50$ nm with different separations S_x are shown in Fig. 2a. For the incident angle larger than the critical angle, the reflectivity drops slowly. Once the horizontal component of the incident wavevector matches that of SPR, the reflectivity reaches the

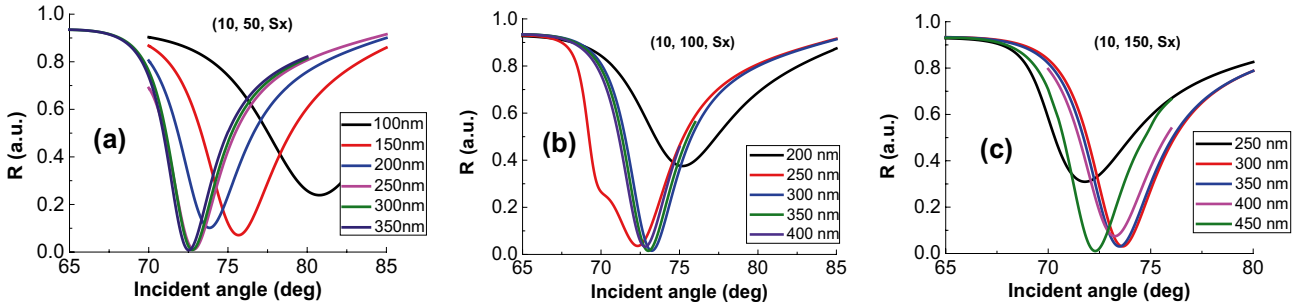

Fig. 2 The SPR reflectivity curves for Au nanodisk arrays at $H = 10$ nm and **a** $D = 50$ nm, **b** 100 nm and **c** 150 nm with different separations S_x between nanodisks

minimum, with the corresponding incident angle known as the SPR angle. As the incident angle continues to increase, the wavevectors are mismatched again, and then the reflectivity starts to rise. Finally, only a reflectivity dip forms in the spectrum, with minimum reflectivity (R_{min}) indicating the maximum energy conversion efficiency between the incident light and surface field. The SPR curve also changes with the spacing between nanodisks, where several changing features in the SPR curve are shown in Fig. 2a. Precisely, the SPR angle decreases as the separation increased, while R_{min} declines rapidly until reaching down to zero with width of the curve also reducing. The optimal separations ($S_x = 250,\ 300,$ and 350 nm) from the above features are easy to be noticed, but the range of optimal separation varies with the basic parameters (H, D) of the nanodisk. At constant H and increased diameter D to 100 nm, the optimal separations are achieved at 300 and 350 nm, equivalent to 450 nm increase for D enlarged to 150 nm. The reflective spectra of Fig. 2b, c reveal a slower increase rate of the optimal separation than that of the nanodisk diameter. The duty cycle of a nanodisk in one unit can be used to indicate this variation, which is approximately represented by the ratio of D and S_x. The optimal separation tends to enlarge with bigger nanodisks, but irrelevant to increase the separation to one wavelength since the duty cycle of the nanodisk becomes larger, while the interface in contact with the analyte solution to be measured becomes more smooth and flat, resulting in constantly weakening of the perturbation effect of nanodisk arrays. Increasing the diameter of the nanodisk would also lead to the same result (Fig. S1b). Therefore, D and S_x are not subjected to an increase in subsequent studies.

The skin depth indicates the influence distance of the SPR field from the sensing interface to the analyte solution. Larger skin depth results in more antigens adsorbed to the antibodies through the SPR field. By considering the non-smooth interface between the sensing chip and analyte solution, the skin depth is extracted at two locations. The first is perpendicular to the center of the nanodisk (q_1), and the second is on the mid-perpendicular line of two adjacent nanodisks (q_2). The skin depths for these configurations with optimal separations at different unit cells are shown in Fig. 3. On the whole, the skin depth shows a downward trend when S_x increases for a given unit cell (H, D). The q_1 value is almost smaller than 200 nm except for $D = 50$ nm and $S_x = 250$ nm, while q_2 value is generally larger than 200 nm, indicating non-uniform field distribution on the interface, as well as different impact depths on antigens. The cross-sectional field distribution of the electric field norm clearly shows these characteristics. As depicted in Fig. 3c, large numbers of charges are gathered at the boundary of each nanodisk forming strong local electric fields, which can adsorb more antigens around. The strong interaction between these electric fields leads to stronger surface field intensity between them than those on the substrate Au film. However, the non-uniformity field intensity distribution along the interface does not last long. The electric field tends to be uniform when entering the analyte solution at about 200 nm. This distance is the same as the skin depth of the SPR field on bare Au film since much more evanescent waves are excited near the nanodisks but decays faster than those on substrate Au film. Greater local field intensities result in faster attenuation along the vertical direction. Finally, a uniform intensity is achieved at a certain distance. The attenuation process can be seen in Fig. 3d. Compared to the attenuation curve of the bare gold film (dotted line), the previous discussion about the evanescent waves can be confirmed. Fortunately, the skin depth at any position is larger than the diameter of the whole coronavirus, meaning that the adsorption of the virus to the chip interface can be fully sensed. By considering the duty cycle of the nanodisk in the current optimized configurations of less than one-third, q_2 is used to represent the skin depth of the sensing system.

Comparing the SPR curves with those of conventional Au and other materials sensing chips is carried out before further analysis of the sensing performance of the Au + Au structure. Figure S2 shows the resulting SPR curves corresponding to Au thin film with and without Au nanodisk arrays. A shift in the curves from right to left is observed, while the

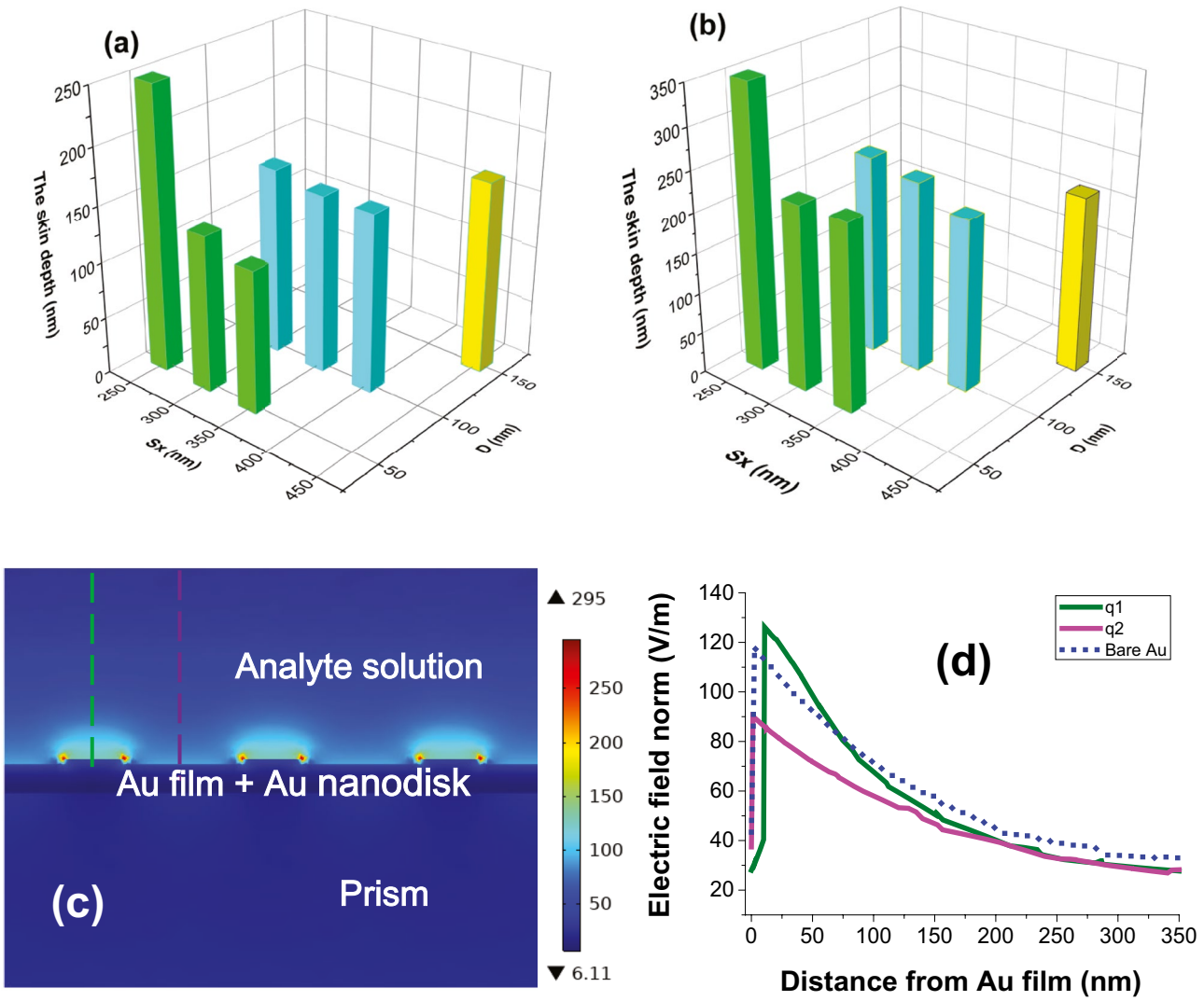

Fig. 3 The skin depth at two locations for optimal separations at different diameters of nanodisks, **a** for q_1 and **b** for q_2. **c** The cross-sectional field distribution of the norm electricity with $D=100$ nm and $S_x=200$ nm at the SPR angle. The dashed lines represent the extracted locations of q_1 and q_2. **d** Electric intensity decays perpendicular to the lower surface of gold penetrating into the analyte solution

width and minimum value remain the same, indicating no degradation of the detection accuracy and coupling efficiency of this 3D-sensing chip by the complexity of the sensing interface. The effects of material properties on the sensing performance are then compared, and two combinations for plasmonic metal replacement are recorded. The first dealt is the complete replacement of Au film and Au nanodisk arrays with other materials, and the second is semi-replacement (Au nanodisk arrays located on a thin film of other material or nanodisk arrays of other material located on Au thin film). The reflective spectra of the complete replacement are presented in Fig. 4b–d and compared with the results of Au + Au in Fig. 4a. The real and imaginary parts of RI of Cu and Pt are both larger than those of Au, indicating worse refractive efficiency at the interface and greater Ohmic loss inside the material. This, in turn, results in a wider characteristic curve in each case and a larger minimum reflectivity R_{min} at SPR angle, especially for Pt. This also shows materials possessing low SPR excitation and conversion efficiencies. On the other hand, though the imaginary part of silver's RI is higher than that of gold to result in R_{min} slightly larger than zero, the real part of RI is much smaller than that of gold. As a result, the FWHM of the spectral line is very small (about 0.75°). Therefore, the detection accuracy can be improved by using Ag as the plasmonic metal. The specific SPR angle and FWHM of each configuration are summarized in Table S1. The comparison reveals the sensing performances of the sensor chips made of gold and silver are better than those made of copper and platinum. Hence, Cu and Pt are no longer considered in further analysis of the sensor chip composition.

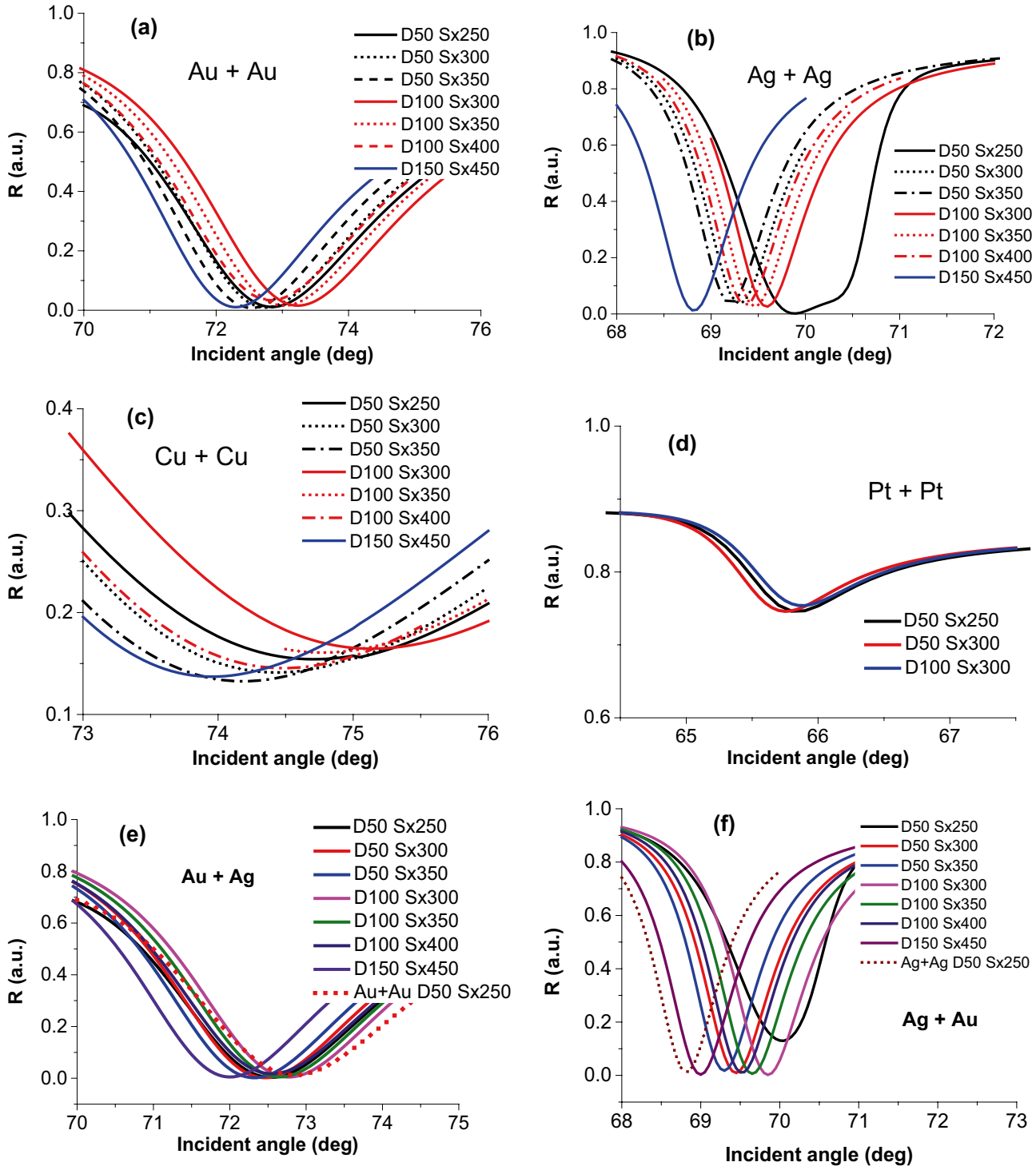

Fig. 4 Reflectivity spectra achieved from the sensor chips with different materials through complement replacements of **a** Au, **b** Ag, **c** Cu, and **d** Pt, and semi-replacements of **e** Au + Ag and **f** Ag + Au

Based on the above data, semi-replacement requires only considering the mixture of gold and silver (a kind of hybrid nanostructure). The starting point of this hybridization is to combine the advantages of gold and silver in terms of sensing performance. Two hybrid nanostructures are considered: Ag nanodisk arrays located on Au thin film (denoted by Au + Ag) and Au nanodisk arrays located on Ag thin film (Ag + Au). The spectral curves of these two hybrid structures are shown

Table 2 The skin depths q_2 (nm) of the sensing chips with different combinations of gold and silver

Parameters (nm)		Au + Au	Au + Ag		Ag + Au		Ag + Ag
		q_2	q_2	FWHM	q_2	FWHM	q_2
D = 50	S_x = 250	350	350	2.95	156	0.90	156
	S_x = 300	228	220	2.75	316	0.85	316
	S_x = 350	230	230	2.70	342	0.80	340
D = 100	S_x = 300	245	267	2.75	360	0.90	360
	S_x = 350	235	238	2.75	350	0.85	360
	S_x = 400	212	212	2.80	331	0.85	330
D = 150	S_x = 450	218	211	2.65	310	0.75	320

in Fig. 4e, f. Regardless of the size of the Ag nanodisks (Fig. 4e), the reflection spectrum shifts only slightly from side to side. Compared to the curve of A + Au, the FWHM of these spectra remains unchanged. However, the other hybrid combination (Ag + Au, Fig. 4f) reveals reduced FWHM of reflective curves for different sizes of nanodisks to about one degree, corresponding to the all-silver situation (Ag + Ag). Hence, the sensing performance of hybrid nanostructures is more dependent on the characteristics of the substrate film. As a result, the nanostructure acting as a perturbation to the interface can control the excitation of the near-field surface waves, but with little effect on the spectrum in the far field.

Furthermore, the near-field parameters are compared to determine the best combination for sensing. The skin depth directly affects the range of physical adsorption of biomolecules. Thus, the skin depth of q_2 is first extracted under different material-parameter combinations, and the values are listed in Table 2. The skin depths of hybrid nanostructures are consistent with those made of the same substrate materials, while the change in nanodisk material does not affect the skin depth at this location. The FWHM of the reflective spectrum with the silver thin film is much smaller than that of the gold thin film, confirming the importance of a continuous thin layer. On the other hand, the near-field effect of nanodisks is obtained from the near-field distribution of the electric field. Figure 5 presents the *E*-field distribution around nanodisks with maximum electric intensity for each combination, which can be seen in the color bar. Interestingly, the nanodisks are all 50 nm in diameter with a separation of about 300–350 nm. This also demonstrates the differences in charge accumulation caused by material properties. Silver nanodisks accumulate fewer charges than gold nanodisks regardless of the material of the substrate film. By comparison, the silver thin film brings stronger field distribution when compared to the gold thin film with the same nanodisks, attributed to the larger conductivity and SPR excitation efficiency of silver than gold. The comprehensive comparison reveals that the combination of Au nanodisks and Au/Ag thin film substrates is more advantages in adsorbing the molecules to be tested, thereby worth further studies.

The changes in SPR angle at variable RI changes of analyte solution from 0 to 0.001 RIU are then calculated under the optimal parameter sets for the combinations of Au and Ag. For both combinations (Fig. 6), the resonance angles under different parameters generally increase with RI except for Ag + Au at $D = 50$ nm and $S_x = 250$ nm with large RI changes. Also, the increments in resonance angle are almost the same. The changes in resonance angle for the combinations of Au + Ag and Ag + Ag (Fig. S3) reveal an almost same increment maintained within 0.2°.

The effect of the aspect ratio (S_x: S_y) of nanodisk arrays on the sensing performance is further investigated. Figure 7 presents the spectrum curves of nanodisk arrays with different S_x: S_y for the configurations of Au + Au and Ag + Au. The effect of aspect ratio on the reflectance spectrum looks

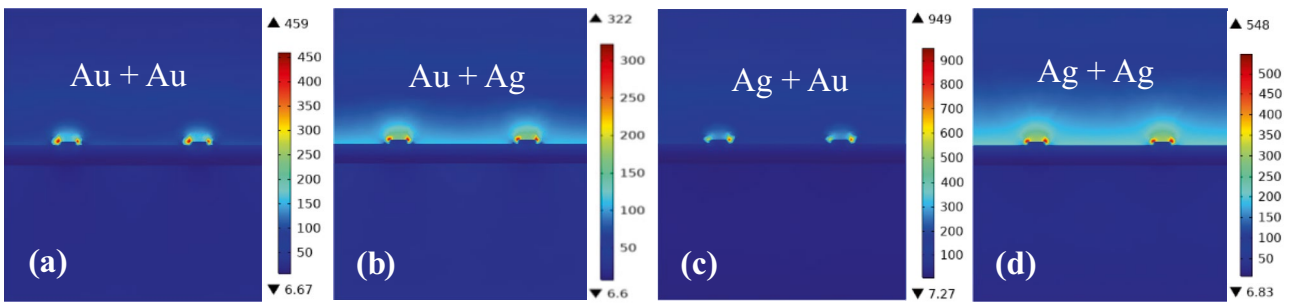

Fig. 5 **a–d** The electric field distributions with maximum intensity for different combinations of Au and Ag

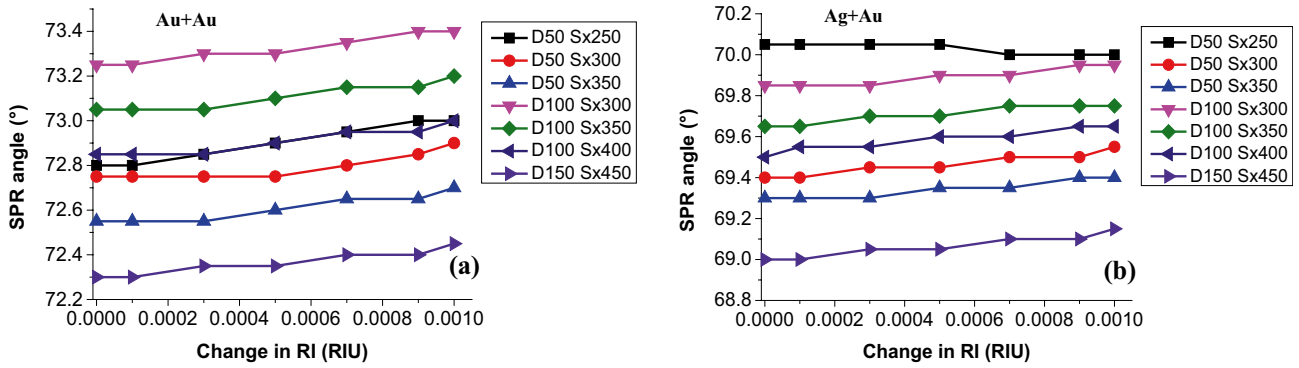

Fig. 6 SPR angle in terms of small RI change of analyte solutions for the combinations of **a** Au + Au and **b** Ag + Au

similar. By taking the square matrix ($S_x = S_y$) as the benchmark at the scale of one side increasing, the reflection spectrum shifts to the left, and vice versa to the right. Since the corresponding resonance angle of some prism-coupled SPR sensor chips is greater than 80°, the detection accuracy is greatly reduced. To adjust the resonance angle, the common method consisting of using other structures or materials with different RI is employed. The improvement in

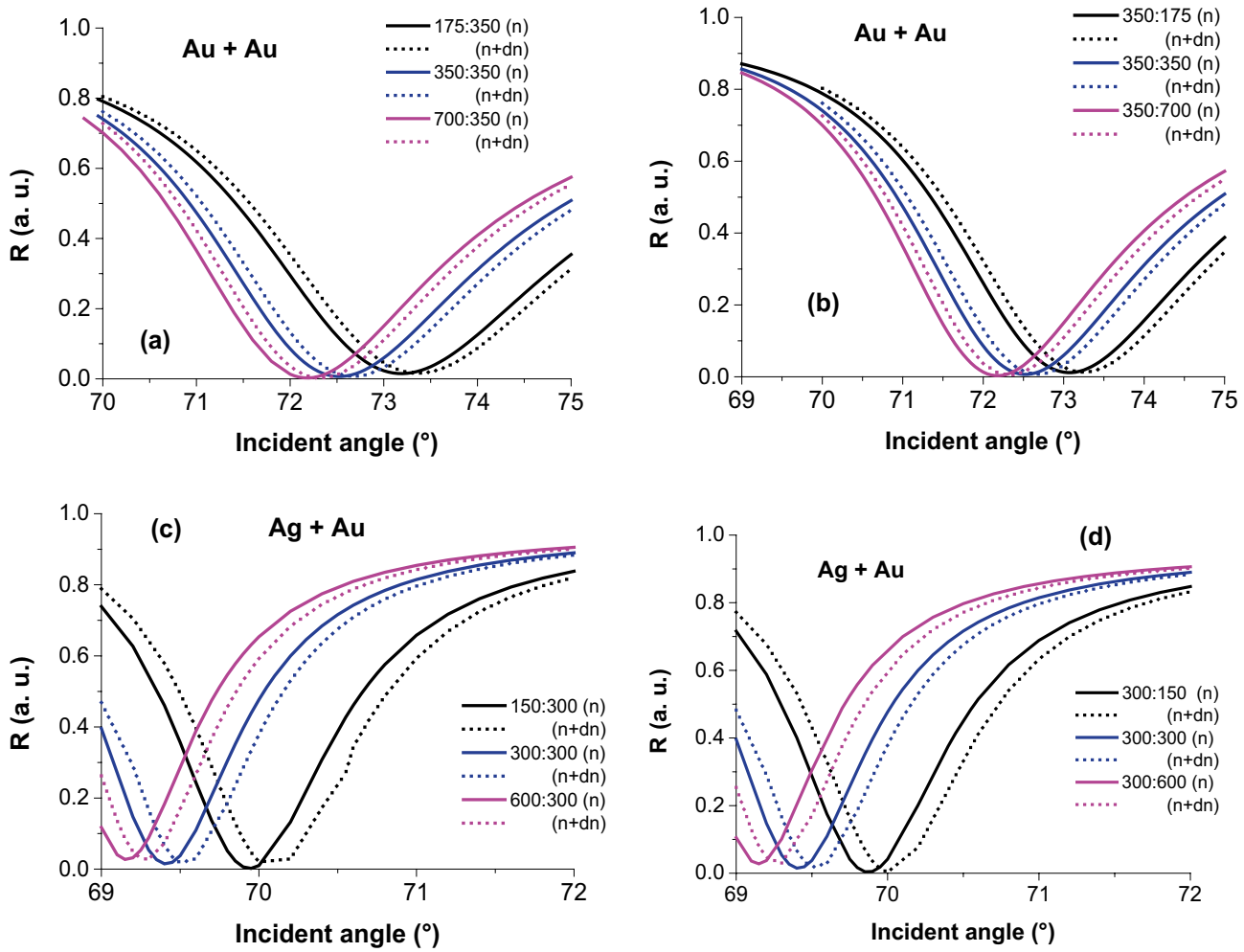

Fig. 7 Reflectivity spectra with the incident angle for the Au + Au configuration at $D = 50$ nm but with different aspect ratios of S_x and S_y. The dotted lines show the reflective curves with the RI change of 0.001 RIU

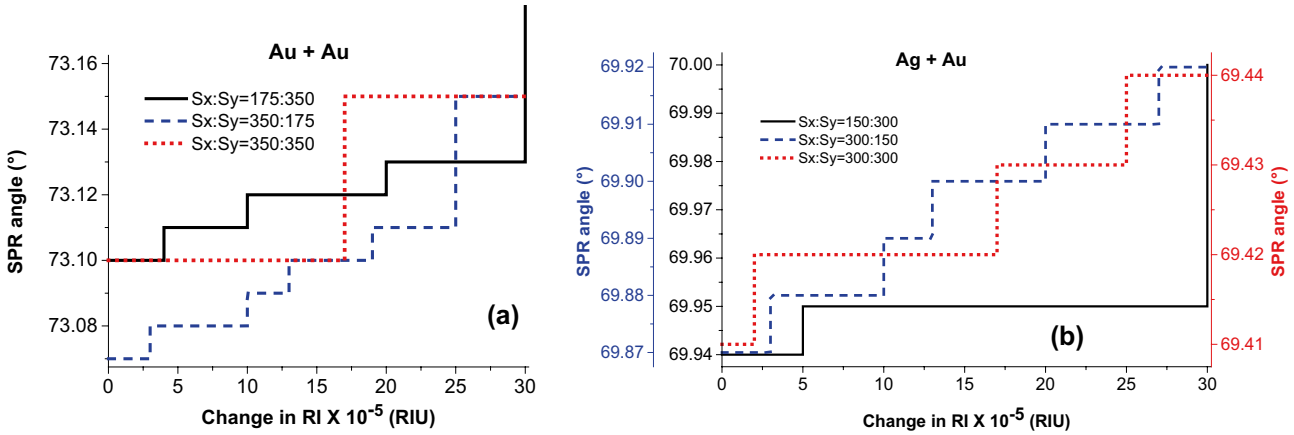

Fig. 8 The change in resonance angle with tiny RI change for **a** Au + Au with the aspect ratio of S_x: S_y = 175:350, 350:175, 350:350 and **b** Ag + Au with S_x: S_y = 150:300, 300:150, 300:300

detection accuracy is often based on reducing other detection performances. Therefore, the resonance angular position is inversely proportional to the ratio of S_x: S_y, actually providing a new way to modulate the reflectance spectrum.

The influence of aspect ratio on the LOD of the sensing system is further studied by selecting configurations with small S_x or S_y, since the corresponding changes in resonance angle with the small RI change of 0.001 are larger than in other cases. The variations in SPR angle with tiny RI changes are provided in Fig. 8. Within the span of RI change ($\Delta n = 0 \sim 3 \times 10^{-4}$ RIU), the variation tendencies look different. For Au + Au case, the LOD reaches as low as 3×10^{-5} RIU with S_x: S_y = 350:175, and the corresponding $\Delta\theta$ reaches 0.01° followed by several RI points causing obvious changes in resonance angle. But the LOD rise to 4×10^{-5} RIU and 17×10^{-5} RIU for S_x: S_y = 175:350 and 350:350, respectively. For the latter case, only one RI change causes a big jump in SPR angle. For the Ag + Au configuration, a lower LOD is achieved at 2×10^{-5} RIU with the square nanodisk array, which increases to3×10^{-5} RIU and 5×10^{-5} RIU, respectively, for rectangular arrays. Overall, the comparison of the variations in SPR angle suggests the advantage of Au + Au configuration with rectangular array distributions of nanodisks not only in terms of low LOD but also for the good detection performance for small RI changes, while the Ag + Au configuration with square or rectangular array distribution achieves similar sensing effects. The multi-jump variations indicate these combinations of the sensor chip can detect the lowest RI change and can clearly distinguish the difference of trace concentrations, which is quite essential to accurately detect trace substances.

The sensitivity, FWHM, FoM, and LOD of these configurations are calculated, and the data are listed in Table 3. The sensitivities for configurations with gold film look always larger than those with silver film for RI change of 0.001 RIU. But the corresponding FoMs are less than half of the latter values due to big FWHM values. But compared with bare Au, the sensitivities of the combination Au + Au are 192% and 154% times. Although the sensitivity for Ag + Au combinations is only 23% higher, the FoM is at least twice higher. The LOD values of all configurations have been reduced to some extent, but remain the same order of magnitude of bare Au, which may be attributed to the fact that the hydrophobicity of plasmonic metals has not been improved due to the nanodisk array.

In addition, the amount of RI change for most commercial sensors caused by the adsorption of ligand and analyte varies in real-time (represented in sensorgram) in experiment. The change of 0.01° in SPR angle corresponds to a variation of 100 RU in the sensorgram response [34]. Hence, the existing commercial sensors can easily detect the theoretical LOD.

The relationship between the concentration of adsorbed molecules and RI can be expressed by the formula:

Table 3 The sensitivity *S*, FoM, and LOD for the configurations of Au + Au and Ag + Au with special aspect ratios of S_x: S_y at RI change of 0.001 RIU. The bare Au is also given for comparison

Configuration	S_x: S_y	*S* (°/RIU)	*FWHM* (°)	*FoM* (RIU^{-1})	*LOD* (RIU)
Au + Au	175:350	250	4.42	56.6	4×10^{-5}
	350:175	200	4.31	46.4	3×10^{-5}
Ag + Au	300:150	150	1.28	117.2	3×10^{-5}
	300:300	150	1.13	132.7	2×10^{-5}
Bare Au	/	130	3.70	35.1	6×10^{-5}

Table 4 Comparison of changes in SPR angle, sensitivity, FoM, and LOD with respect to the design strategy among published sensors and the present sensor

Configuration	Wavelength (nm)	S [°/RIU]	FoM [RIU^{-1}]	LOD [RIU]	Reference
Au nanorod with Au film	830	111.11	/	7×10^{-5}	[37]
Au/$PtSe_2$/graphene	632.8	183.33	47	/	[27]
Ag/$MoSe_2$/graphene	/	194	54.039	/	[17]
Au nanodisks on Ag film	633	150	131.6	2×10^{-5}	Current work
Au nanodisks on Au film	633	250	56.4	4×10^{-5}	

$n = 1.3326 + C\frac{dn}{dc}$, where C is the concentration of adsorbed molecules and $\frac{dn}{dc}$ denotes the increment factor of RI considered as 0.181 cm^3/gm for water [35, 36]. The concentrations corresponding to the above four LOD are then calculated. For the lowest concentration of SARS-CoV-2 detected in the range of 110.5–221 μg/cm^3, the person is confirmed to be infected with virus. If the analyte solution is not pure, we can add a biofunctionalization nanosheet of ACE2 to screen SARS-CoV-2 virus particles from others. We can also change the biofunctionalized nanosheet to detect other viruses but it is beyond the scope of this work.

Finally, the present results are compared with other published works about virus detection, and the results are listed in Table 4. The sensitivity and detection limit of our work are larger than others, indicating good sensing performance of our sensing scheme.

Conclusions

The mutation and iteration of SARS-CoV-2 decline its toxicity while exponentially increase its transmissibility. Thus, early detection of the virus may block its spread between humans by isolating or increasing social distance. In this work, a nanodisk array located on a plasmonic metallic thin film was employed to form sensing substrates for enhancing RI detection sensitivity thanks to the real-time and label-free detection characteristics of SPR. The surface field around the nanodisks was quite stronger than in other places, resulting in extremely sensitive SPR angle to RI changes caused by adsorbing SARS-CoV-2 virus present in the aqueous solution near the sensing interface. The simulation results were provided for various nanodisk arrangements and plasmonic metals. The data revealed configurations of gold nanodisk on silver or gold thin film were more sensitive to the RI change, and the highest sensitivity is about twice that of bare gold. The nanodisk should be small, acting like a perturbation on the thin film. The aspect ratio of nanodisk distribution significantly impacted the sensing results and can flexibly modulate the resonance angle position. Especially, the multi-jump resonance angle curves at tiny refractive index can clearly distinguish the difference of trace concentrations, which is very important for the accurate detection of trace substances.

Supplementary Information The online version contains supplementary material available at https://doi.org/10.1007/s11468-023-01802-3.

Author Contribution All authors contributed to the study. Guo Yan wrote the main manuscript. Su Xianglong prepared Table 4. Yong Ken Tye and Wu kaihua put forward suggestions for improvement.

Funding This work was supported by the National Natural Science Foundation of China (grant no. 11304070).

Data Availability The data underlying the results presented in this paper are not publicly available at this time but may be obtained from the corresponding authors upon reasonable request.

Declarations

Competing Interests The authors declare no competing interests.

References

1. Su S, Wong G, Shi W, Liu J, Gao GF (2016) Epidemiology, genetic recombination, and pathogenesis of coronaviruses. Trends Microbiol 24:490–502
2. Zhu N, Zhang D, Wang W, Li X, Yang B, Song J, Zhao X, Huang B, Shi W, Lu R, Niu P, Zhan F, Ma X, Wang D, Xu W, Wu G, Gao G, Tan W (2020) A novel coronavirus from patients with pneumonia in China, 2019. N Engl J Med 382:727–733
3. de Wit E, van Doremalen N, Falzarano D, Munster VJ (2016) SARS and MERS: recent insights into emerging coronaviruses. Nat Rev Microbiol 14:523–534
4. Wrapp D, Wang N, Corbett KS, Goldsmith JA, Hsieh CL, Abiona O, Graham BS, Mclellan JS (2020) Cryo-EM structure of the 2019-nCoV spike in the prefusion conformation. Science 367:1260
5. Weiss C, Carriere M, Fusco L, Capua I, Regla-Nava JA, Pasquali M, Scott JA, Vitale F, Unal MA, Mattevi C, Bedognetti D, Merkoci A, Tasciotti E, Yilmazer A, Gogotsi Y, Stellacci F, Delogu LG (2020) Toward nanotechnology-enabled approaches against the COVID-19 pandemic. ACS Nano 14:6383–6406
6. Suzuki R, Yamasoba D, Kimura I, Wang L, Kishimoto M, Ito J, Morioka Y, Nao N, Nasser H, Uriu K (2022) Attenuated fusogenicity and pathogenicity of SARS-CoV-2 omicron variant. Nature 603(7902):700–705
7. Zhong JF, Weiner LP, Burke K, Taylor CR (2007) Viral RNA extraction for in-the-field analysis. J Virol Methods 144(1–2):98–102
8. Mulder J, McKinney N, Christopherson C, Sninsky J, Greenfield L, Kwok S (1994) Rapid and simple PCR assay for quantitation of human immunodeficiency virus type 1 RNA in plasma: application to acute retroviral infection. J Clin Microbiol 32:292–300
9. Berger A, Braner J, Doerr HW, Weber B (1998) Quantification of viral load: clinical relevance for human immunodeficiency virus, hepatitis B virus and hepatitis C virus infection. Intervirology 41:24–34

10. Boeckh M, Boivin G (1998) Quantitation of cytomegalovirus: methodologic aspects and clinical applications. Clin Microbiol Rev 11:533–554
11. Paulij WP, de Wit PLM, Sünnen CMG, van Roosmalen MH, Petersenvan Ettekoven A, Cooreman MP, Heijtink RA (1999) Localization of a unique hepatitis B virus epitope sheds new light on the structure of hepatitis B virus surface antigen. J Gen Virol 80(Pt 8)(12):2121
12. Butt SA, Maceira VP, McCallen ME, Stellrecht KA (2014) Comparison of three commercial RT-PCR systems for the detection of respiratory viruses. J Clin Virol 61:406–410
13. Piralla A, Daleno C, Pariani E, Conaldi P, Esposito S, Zanetti A, Baldanti F (2013) Virtual quantification of influenza A virus load by real-time RT-PCR. J Clin Virol Official Publ Pan Am Soc Clin Virol 56(1):65–68
14. Baac H, Hajós JP, Lee J, Kim D, Kim SJ, Shuler ML (2006) Antibody-based surface plasmon resonance detection of intact viral pathogen. Biotechnol Bioeng 94(4):815–819
15. Zheng S, Kim DK, Park TJ, Lee SJ, Sang YL (2010) Label-free optical diagnosis of hepatitis B virus with genetically engineered fusion proteins. Talanta 82(2):803–809
16. Keske A, Atar A, Üstündağ İ, Çağlayan MO (2014) Detection of influenza A by surface plasmon resonance enhanced total internal reflection ellipsometry. J Comput Theor Nanos 11(4):981–986
17. Kim SA, Byun KM, Kim K, Jang SM, Ma K, Oh Y, Kim D, Kim SG, Shuler ML, Kim SJ (2010) Surface-enhanced localized surface plasmon resonance biosensing of avian influenza DNA hybridization using subwavelength metallic nanoarrays. Nanotechnology 21(35):355503
18. Yang ZW, Pham TT, Hsu CC, Lien CH, Phan QH (2022) Single-layer-graphene-coated and gold-film-based surface plasmon resonance prism coupler sensor for immunoglobulin G detection. Sensors 22(4):1362
19. Song W, Wang Y, Wang N, Wang D, Guo J, Fu L, Shi X (2014) Identification of residues on human receptor DPP4 critical for MERS-CoV binding and entry. Virology 471–473:49–53
20. Park TJ, Hyun MS, Lee HJ, Sang YL, Ko S (2009) A self-assembled fusion protein-based surface plasmon resonance biosensor for rapid diagnosis of severe acute respiratory syndrome. Talanta 79(2):295–301
21. Lu R, Zhao X, Li J, Niu P, Yang B, Wu H, Wang W, Song H, Huang B, Zhu N, Bi Y, Ma X, Zhan F, Wang L, Hu T, Zhou H, Hu Z, Zhou W, Zhao L, Chen J, Meng Y, Wang J, Lin Y, Yuan J, Xie Z, Ma J, Liu WJ, Wagn D, Xu W, Holmes EC, Gao GF, Wu G, Chen W, Shi W, Tan W (2020) Genomic characterisation and epidemiology of 2019 novel coronavirus: implications for virus origins and receptor binding. Lancet 395:565–574
22. Chi X, Yan R, Zhang J, Zhang G, Zhang Y, Hao M, Zhang Z, Fan P, Dong Y, Yang Y, Chen Z, Guo Y, Zhang J, Li Y, Song X, Chen Y, Xia L, Fu L, Hou L, Xu J, Yu C, Li J, Zhou Q, Chen W (2020) A neutralizing human antibody binds to the N-terminal domain of the spike protein of SARS-CoV-2. Science 369(6504):650–655
23. Coronaviridas Study Group of the International Committee on Taxonomy of Viruses (2020) The species severe acute respiratory syndrome-related coronavirus: classifying 2019-nCoV and naming it SARS-CoV-2. Nat Microbiol 5:536–544
24. Wrapp D, Wang N, Corbett KS, Goldsmith JA, Hsieh CL, Abiona O, Graham BS, McLellan JS (2020) Cryo-EM structure of the 2019-nCoV spike in the prefusion conformation. Science 367(6483):1260–1263
25. Long QX, Liu BZ, Deng HJ, Wu G, Deng K, Chen Y, Liao P, Qiu J, Lin Y, Cai X, Wang D, Hu Y, Ren J, Tang N, Xu Y, Yu L, Mo Z, Gong F, Zhang X, Tian W, Hu L, Zhang X, Xiang J, Du H, Liu H, Lang C, Luo X, Wu S, Cui X, Zhou Z, Zhu M, Wang J, Xue C, Li X, Wang L, Li Z, Wang K, Niu C, Yang Q, Tang X, Zhang Y, Liu X, Li J, Zhang D, Zhang F, Liu P, Yuan J, Li Q, Hu J, Chen J, Huang A (2020) Antibody responses to SARS-CoV-2 in patients with COVID-19. Nat Med 26:845–848
26. Letko M, Marzi A, Munster V (2020) Functional assessment of cell entry and receptor usage for SARS-CoV-2 and other lineage B betacoronaviruses. Nat Microbiol 5:562–569
27. Akib TBA, Mou SF, Rahman MM, Rana MM, Kouzani AZ (2021) Design and numerical analysis of a graphene-coated SPR biosensor for rapid detection of the novel coronavirus. Sensors 21:3491
28. Uddin SMA, Chowdhury SS, Kabir E (2021) Numerical analysis of a highly sensitive surface plasmon resonance sensor for SARS-CoV-2 detection. Plasmonics 16(6):2025–2037
29. Moznuzzaman M, Khan I, Islam MR (2021) Nano-layered surface plasmon resonance-based highly sensitive biosensor for virus detection: a theoretical approach to detect SARS-CoV-2. AIP Adv 11(6):065023
30. Zheng YQ, Bian SM, Rong G (2022) Label-free LSPR-vertical microcavity biosensor for on-site SARS-CoV-2 detection. Biosensors 12(3):151
31. Shen Y, Zhou J, Liu T, Tao Y, Jiang R, Liu M, Xiao G, Zhu J, Zhou Z, Wang X, Jin C, Wang J (2013) Plasmonic gold mushroom arrays with refractive index sensing figures of merit approaching the theoretical limit. Nat Commun 4:2381
32. Qiu G, Gai Z, Tao Y, Schmitt J, Kullak-Ublick GA, Wang J (2020) Dual-functional plasmonic photothermal biosensors for highly accurate severe acute respiratory syndrome coronavirus 2 detection. ACS Nano 14:5268–5277
33. Ta Y, Kajisa T, Ono M, Miyasaka Y, Hasegawa Y, Saito A, Otsuka K, Sakane A, Sasaki T, Yasutomo K, Hamajima R, Kanai Y, Kobayashi T, Matsuura Y, Itonaga M, Yasui T (2022) Ultrasensitive detection of SARS-CoV-2 nucleocapsid protein using large gold nanoparticle enhanced surface plasmon resonance. Sci Rep 12:1060
34. Ravi Shankaran R, Miura N (2007) Trends in interfacial design for surface plasmon resonance based immunoassays. J Phys D Appl Phys 40(23):7187–7200
35. Hossain MB, Khan MMR, Rahman MS, Badrudduza SSB, Sabiha MM, Rana MM (2019) Graphene-MoS_2-Au-TiO_2-SiO_2 hybrid SPR biosensor: a new window for formalin detection. J Mater Appl 8(2):51–58
36. Rahman MS, Hasan M, Rikta KA, Anower MS (2018) A novel graphene coated surface plasmon resonance biosensor with tungsten disulfide (WS_2) for sensing DNA hybridization. Opt Mater 75:567–573
37. Das CM, Guo Y, Yang G, Kang LX, Xu GX, Ho HP, Yong KT (2020) Gold nanorod assisted enhanced plasmonic detection scheme of COVID-19 SARS-CoV-2 spike protein. Adv Theory Simul 3(11):2000185